Title
Negative membrane curvature catalyzes nucleation of endosomal sorting complex required for transport (ESCRT)-III assembly

Journal
Proceedings of the National Academy of Sciences of the United States of America, 112(52)

ISSN
0027-8424

Authors
Lee, Il-Hyung
Kai, Hiroyuki
Carlson, Lars-Anders
et al.

Publication Date
2015-12-29

DOI
10.1073/pnas.1518765113

Peer reviewed

Negative membrane curvature catalyzes nucleation of endosomal sorting complex required for transport (ESCRT)-III assembly

Il-Hyung Lee[a,b], Hiroyuki Kai[b,c], Lars-Anders Carlson[a,b], Jay T. Groves[b,c,d,e,f], and James H. Hurley[a,b,e,1]

[a]Department of Molecular and Cell Biology, University of California, Berkeley, CA 94720; [b]California Institute for Quantitative Biosciences, University of California, Berkeley, CA 94720; [c]Department of Chemistry, University of California, Berkeley, CA 94720; [d]Molecular Biophysics and Integrated Bioimaging Division, Lawrence Berkeley National Laboratory, Berkeley, CA 94720; [e]Materials Sciences Division, Lawrence Berkeley National Laboratory, Berkeley, CA 94720; and [f]Mechanobiology Institute, National University of Singapore, Singapore 117411

Edited by David Baker, University of Washington, Seattle, WA, and approved November 20, 2015 (received for review September 21, 2015)

The endosomal sorting complexes required for transport (ESCRT) machinery functions in HIV-1 budding, cytokinesis, multivesicular body biogenesis, and other pathways, in the course of which it interacts with concave membrane necks and bud rims. To test the role of membrane shape in regulating ESCRT assembly, we nanofabricated templates for invaginated supported lipid bilayers. The assembly of the core ESCRT-III subunit CHMP4B/Snf7 is preferentially nucleated in the resulting 100-nm-deep membrane concavities. ESCRT-II and CHMP6 accelerate CHMP4B assembly by increasing the concentration of nucleation seeds. Superresolution imaging was used to visualize CHMP4B/Snf7 concentration in a negatively curved annulus at the rim of the invagination. Although Snf7 assemblies nucleate slowly on flat membranes, outward growth onto the flat membrane is efficiently nucleated at invaginations. The nucleation behavior provides a biophysical explanation for the timing of ESCRT-III recruitment and membrane scission in HIV-1 budding.

membrane bending | HIV-1 | nanofabrication | superresolution imaging

The endosomal sorting complexes required for transport (ESCRTs) are an ancient and conserved system for membrane scission (1, 2). ESCRT membrane remodeling activities are important in the budding of HIV-1 and other viruses from host cell membranes (3); cytokinesis (4); lysosomal transport (5); and more recently discovered functions that include membrane repair, exosome biogenesis, and nuclear envelope reformation (6). The ESCRTs are unique in that they promote membrane budding and sever membrane necks by working from the inner face of the bud (1, 2).

The ESCRTs consist of the upstream complexes ESCRT-I, ESCRT-II, and ALIX, which recognize cargo, the ESCRT-III complex responsible for membrane scission, and the AAA+ ATPase VPS4, which releases and recycles ESCRT-III (1, 2). In this study, we focus on the human ESCRT-III subunit CHMP4B, which is considered a core component of the membrane scission machinery and is essential for HIV-1 budding (7). Its yeast counterpart is Snf7. CHMP4 can be recruited and activated through two different pathways in human cells. The first proceeds through ESCRT-I, ESCRT-II, and CHMP6, and the second through ALIX (3). The ESCRT-II– and CHMP6-dependent pathway functions downstream of ESCRT-I, which is in turn the essential link between HIV-1 Gag and the ESCRTs (3). Although there is uncertainty over whether ESCRT-II itself is essential in HIV-1 budding, the most recent virological data suggest that ESCRT-II is important for the efficient release of HIV-1 (8). Moreover, ESCRT-II and CHMP6 were required to bridge Gag and ESCRT-I to the rest of ESCRT-III in a reconstituted system (9).

Most concepts of ESCRT recruitment to HIV-1 budding sites have focused on protein–protein interactions between the PTAP and YPXL late domain motifs of the Gag p6 domain and ESCRT-I and ALIX, respectively (3). ESCRT-I is recruited to HIV-1 budding sites simultaneously with Gag (10). However, ESCRT-III is recruited after a time lag and only to Gag that has already assembled on the plasma membrane (10, 11). In principle, either the oligomerization of Gag or its membrane association might trigger ESCRT-III recruitment to Gag-ESCRT-I assemblies. In one recent report, ESCRT-III assembly was visualized by superresolution light microscopy within the center of the Gag shell (12). This observation led to a model for virus scaffolding of ESCRT-III assembly, which downplayed the direct role of membrane shape. Another group, also using superresolution imaging, noted a displacement of the ESCRT-III localization closer to the plasma membrane than the mean position of Gag (13), consistent with ESCRT-III localization predominantly to the bud neck (3). The latter model implies that ESCRT-III could be a coincidence detector, responsive both to the presence of upstream interacting proteins and to membrane shape. Whereas an abundant literature describes the role of viral late domains and other protein interactions in ESCRT recruitment, almost no data are available on the role of membrane curvature in initiating ESCRT-III assembly.

In this study, we set out to characterize the recruitment and assembly of purified ESCRT complexes on membranes of a defined geometry approximating that of an early stage HIV-1 budding site. At early stages, budding profiles with broad necks have been visualized in thin-section EM and in cryo-EM tomograms (14–17). During the process of their formation, HIV-1 budding intermediates are 50–100 nm deep and slightly over 100 nm wide. The well-developed methods for studying protein interactions with positively curvature membranes (18) cannot be applied to this type of geometry. Here, we used a focused ion beam to fabricate a 100-nm-deep invaginated template for negative curvature, which approximates the shape of a nascent

Significance

The endosomal sorting complex required for transport (ESCRT) proteins remodel and sever membranes in a wide range of biology, including HIV budding. Electron microscopy has shown that ESCRT-III is often found in contact with concave (negatively curved) membrane surfaces. It has not been possible until now to determine whether the ESCRTs have an inherent preference for binding to concave membrane because it is difficult to make nanoscale concave membranes. Here we have made such membranes on the dimensions of an HIV budding site. We show that ESCRT-III assembly begins (nucleates) much faster on concave membranes, which explains why this complex is recruited in a rapid burst late in HIV budding.

Author contributions: I.-H.L., J.T.G., and J.H.H. designed research; I.-H.L. performed research; I.-H.L., H.K., and L.-A.C. contributed new reagents/analytic tools; I.-H.L. and J.H.H. analyzed data; and I.-H.L. and J.H.H. wrote the paper.

The authors declare no conflict of interest.

This article is a PNAS Direct Submission.

[1]To whom correspondence should be addressed. Email: jimhurley@berkeley.edu.

This article contains supporting information online at www.pnas.org/lookup/suppl/doi:10.1073/pnas.1518765113/-/DCSupplemental.

HIV-1 bud. When coated with a supported lipid bilayer, we term this structure an invaginated supported lipid bilayer (invSLB). We went on to measure CHMP4B/Snf7 assembly in real time, which allowed us to dissect in vitro, and in real time, the role of membrane shape in the nucleation and growth of ESCRT polymers.

Results

The invSLB. We fabricated a membrane substrate of appropriate topology, the invSLB, to study the assembly of ESCRTs on negatively curved membranes (Fig. 1). We used a focused ion beam to excavate concavities in glass coverslips using a target cylindrical milling shape set to 100 nm in radius and 100 nm in depth, and spaced 5 μm apart on a grid. The invaginations were characterized by atomic force microscopy (AFM; Fig. 1 *A–C* and *SI Appendix*, Fig. S1 *A* and *B*). The intended depth was attained, and the typical radius of the concavities was 250 nm. Supported lipid bilayers (SLBs) (19) were formed by spontaneous rupture of lipid vesicles on clean fabricated glass surfaces. It was previously shown in a study of zero mode waveguides coated with lipid bilayers that liquid phase bilayers follow the contour of preformed 50- to 200-nm invaginations (20). We carried out fluorescence recovery after photo-bleaching (FRAP) using the membrane-incorporated dye DiD (1,1′-dioctadecyl-3,3,3′,3′-tetramethylindodicarbo-cyanine perchlorate), which showed a complete recovery of fluorescence. The observation of recovery confirmed that the invSLB membrane was continuous and fluid (Fig. 1*D*).

CHMP4B Proteins Preferentially Cluster into Invaginations. When we added Atto488 labeled CHMP4B in solution phase above the invSLB, we observed preferential recruitment of CHMP4B to the invaginations (Fig. 2*A*). We could clearly recognize the regular 5-μm grid pattern of the invagination from the protein fluorescence. We performed incubation experiments with different lipid compositions to test the dependence of recruitment on membrane composition. We quantified the mean fluorescence emission intensity at invaginations for each lipid composition (Fig. 2*B*). Fig. 2*C* shows that the peak Atto488-CHMP4B intensity is six- to ninefold higher in invaginations than in the surrounding flat SLB. Recruitment to invaginations required the presence of negatively charged lipids. To determine whether PS was selectively recruited to invaginations, we quantitated the TopFluor tail-labeled PS (*SI Appendix*, Fig. S2). TopFluor intensity was not enriched beyond the proportion expected from the additional surface area of the invagination. The neutral lipid PC did not recruit CHMP4B (Fig. 2*B*). Recruitment of CHMP4B in isolation of other ESCRT subunits is therefore not significantly different between PC:PS:PI3P and PC:PS (85:15) (Fig. 2*B*), showing that net negative charge is more important than the particular lipid composition.

As a control for nonspecific interaction with membrane defects either at the invaginations or elsewhere, we incubated invSLBs with Atto488-ubiquitin (Fig. 2*D* and *SI Appendix*, Fig. S3 *A* and *E*), a protein that is not expected to bind membranes at all. Atto488-ubiquitin produced a minimal signal, <5% that of 400 nM CHMP4B. Similarly, Cy3-BSA showed a minimal signal at the invaginations. Cy5-His_6-ubiquitin was tethered to an invSLB containing Ni-NTA-DOGS. Tethered Cy5-His_6-ubiquitin was more or less uniformly distributed on the membrane surface, irrespective of the invaginations (*SI Appendix*, Fig. S3*B*).

Bin-Amphiphysin-Rvs (BAR) domains bind to positively curved membranes (18, 21), and the BAR domain protein angiomotin was recently shown to localize to nascent HIV-1 buds (17). The sorting nexin SNX1 consists of an N-terminal unstructured region, a PX domain, and an N-BAR domain (22). Constructs including the N-BAR domain bind tightly to curved membranes (22). Consistent with the previous finding that the isolated BAR domain lacking the N-terminal helix did not bind to curved membranes, this construct interacted with the invSLB (PC:PS:PI3P) at background level (Fig. 2*D* and *SI Appendix*, Fig. S2*C*), even at 400 nM. The SNX1 PX-N-BAR construct bound to the PC:PS:PI3P invSLB above background but below the level of CHMP4B (Fig. 2*D* and *SI*

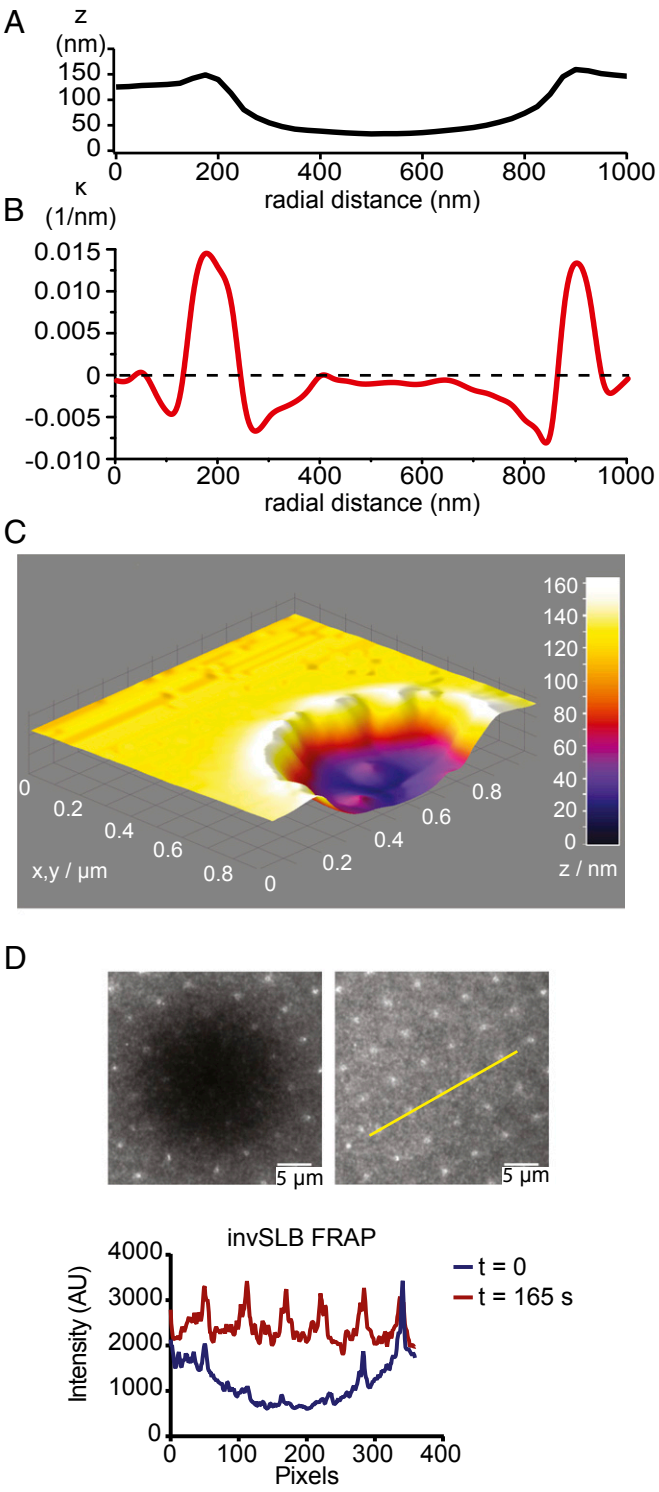

Fig. 1. Characterization of invSLBs. (*A*) A representative line profile of the nanofabricated glass surface. The geometries shown are actual morphologies measured by atomic force microscopy. (*B*) Curvature (κ) in the plane of the plotting section calculated from the same morphology as an inverse of the radius of the osculating circle. (*C*) 3D surface plot of the AFM measurement. (*D*) Fluorescence recovery after photobleaching of the invSLB. 0.005% DiD in the SLB was monitored in time steps of 15 s. The fluidic nature of the membrane is clear from full recovery after 165 s both in the flat and invaginated regions of the membrane. (Scale bars, 5 μm.)

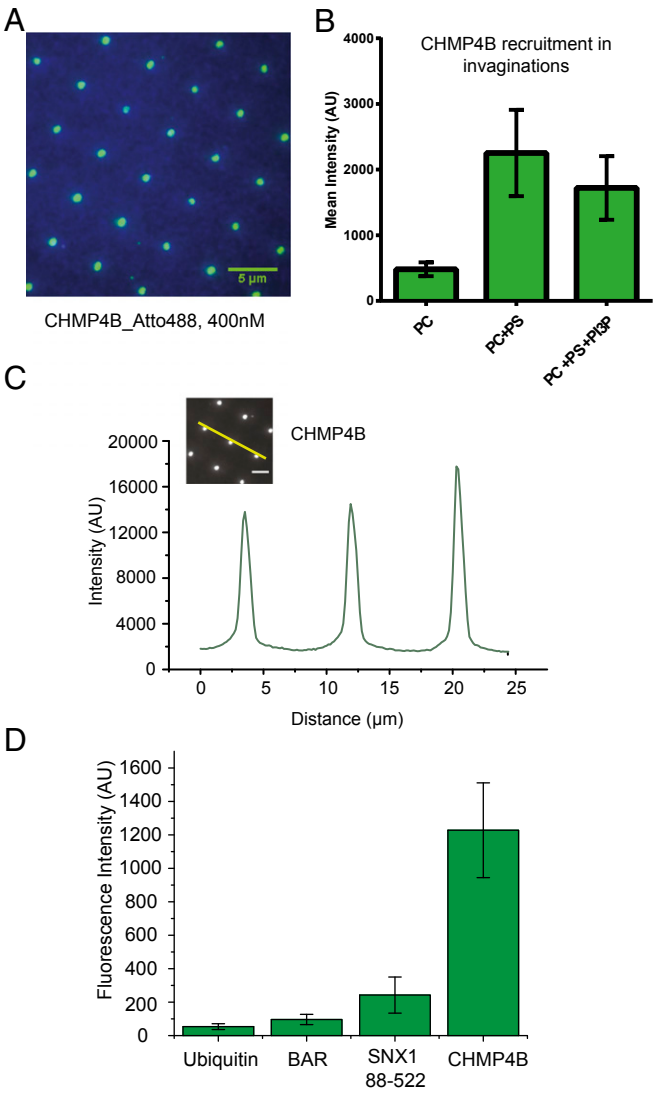

Fig. 2. Preferential recruitment of CHMP4B to invaginations. (*A*) TIRF fluorescence image after 20-min incubation with 400 nM CHMP4B-Atto488. Green, Atto488 fluorescence channel; blue, DiD fluorescence, where DiD is used as a marker for lipids. (*B*) Quantification of average fluorescence recruitment in invaginations at different lipid compositions. The mean intensity around invaginations after 20-min incubation was averaged. Error bars indicate SDs of averages over multiple invaginations. (*C*) A representative intensity profile (yellow line) from the 400 nM CHMP4B incubation with PC, PS, and PI3P. (*D*) Quantified average fluorescence intensity on invaginations of different fluorescently lagged proteins. BAR domain binding is similar to nonspecific binding. Example images of each experiment are shown in *SI Appendix*, Fig. S3.

Appendix, Fig. S3 *D* and *G*). The intermediate level of binding for the SNX1 construct is consistent with the presence of positive curvature at the rim of the invagination, but the predominance of negative curvature overall. The overall conclusion of these experiments is that CHMP4 binds strongly and specifically to the invaginations.

ESCRT-II and CHMP6 Accelerate CHMP4B Cluster Nucleation. We performed CHMP4B recruitment experiments as a function of concentration and monitored the kinetics of intensity gain at invaginations (Fig. 3 *A* and *B*, *SI Appendix*, Fig. S4 *A* and *B* and Table S1, and Movie S1). We observed a sigmoidal increase of CHMP4B intensity as a function of time. We interpreted this behavior as involving a nucleation step and a growth step. The activation of CHMP4B by ESCRT-II and CHMP6 is one of the best-characterized events in the ESCRT pathway (23–27), and we therefore choose it as the most appropriate vehicle to compare behavior in the invSLB setting to past results. We sought to determine whether ESCRT-II and CHMP6 affected CHMP4B polymer nucleation or growth or the total amount of CHMP4 deposited. Fluorescence intensity values around the invaginations were measured and averaged for each time point (Fig. 4 and *SI Appendix*, Fig. S5 *A* and *B* and Table S2). We quantified CHMP4B clustering kinetics in the presence and absence of ESCRT-II and CHMP6. We carried out 20-min tracking experiments for each situation, with 100 nM ESCRT-II and 200 nM CHMP6 either coincubated with CHMP4B or omitted. When we quantified the total amount of CHMP4B recruited in invaginations at equilibrium, we found that ESCRT-II and CHMP6 had little effect on the final values (Fig. 4*A*). On the other hand, when we quantified the kinetics of intensity gain, we found different lag times. The lag phase was followed by a steep increase in intensity at an approximately constant rate (Fig. 4*B*). The sigmoidal recruitment saturation was followed by decrease of signal due to photobleaching, even with presence of an oxygen scavenger system. The data showed that the upstream components ESCRT-II and CHMP6 acted primarily by decreasing the lag time preceding polymerization. A threefold increase in the growth rate was also noted, which could represent a secondary activation mode. These data show that ESCRT-II and CHMP6 are nucleation and growth catalysts for CHMP4B.

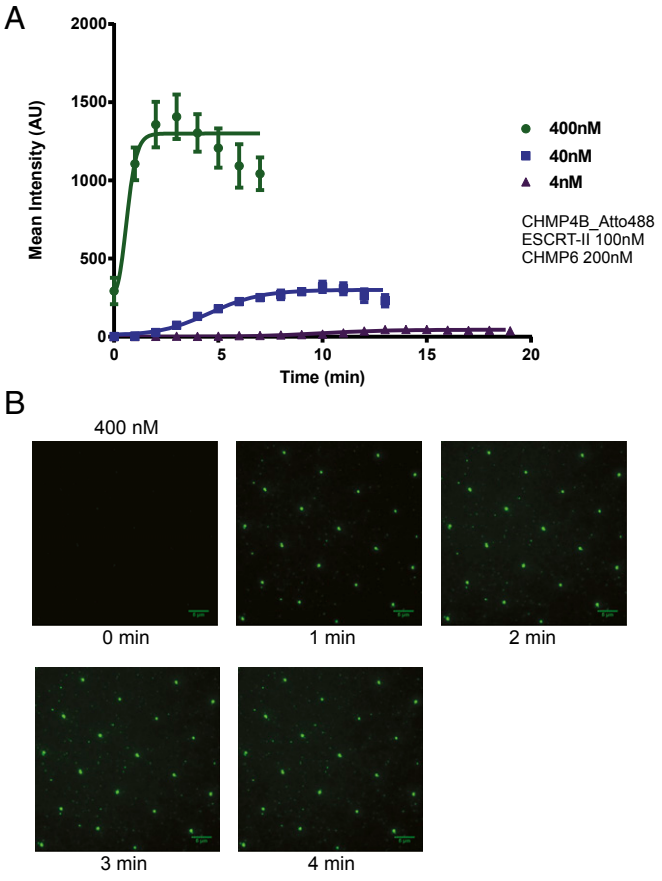

Fig. 3. Sigmoidal kinetics of CHMP4B recruitment to invaginations. (*A*) Mean fluorescence intensity within a 0.9-μm radius of the invaginations was averaged for each time point from 20-min time lapse image stacks of the Atto488 fluorescence channel; 100-ms exposure images at multiple positions were acquired every 1 min. Five randomly chosen invaginations were analyzed for each position, and multiple time lapse stacks from different positions were averaged. Error bars represent SDs ESCRT-II (100 nM) and 200 nM CHMP6 were coincubated with the indicated amount of CHMP4B-Atto488. (*B*) Representative time lapse images of the 400 nM CHMP4B-Atto488 experiment. Further images are shown in *SI Appendix*, Fig. S4. (Scale bars, 5 μm.)

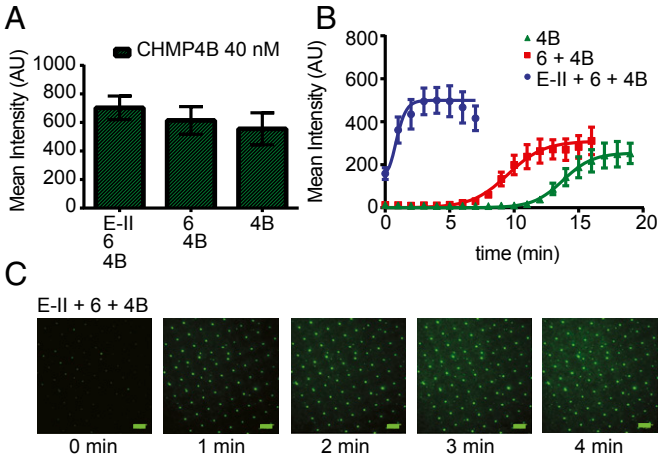

Fig. 4. ESCRT-II and CHMP6 promote CHMP4B nucleation. (*A*) Average protein fluorescence within a 1.3-μm zone about each invagination after 20-min incubation with and without 100 nM ESCRT-II and 200 nM CHMP6 as indicated. Error bars represent SD. (*B*) Kinetic traces of the same experiments. Quantitation was carried out as for Fig. 3. Error bars represent SDs. ESCRT-II (100 nM) and 200 nM CHMP6 were coincubated with 40 nM CHMP4B-Atto488. (*C*) Representative time lapse images of of the ESCRT-II + CHMP6+ CHMP4B-Atto488 experiment. Further images are shown in *SI Appendix*, Fig. S5. (Scale bars, 5 μm.)

We interpreted the data in terms of the following quantitative model for nucleation and growth of the ESCRT-III polymer, adapted from previous work on amyloid polymerization (28). In the model, growth proceeds by linear addition of monomers to the growing end or ends of the polymer. Here, $[E]$ denotes the concentration of elongation ends, $[A_1]$ is the free monomer concentration, $[A_{tot}]$ is the total protein concentration in the invagination, k_n is the rate constant for the nucleation reaction, and k_e is the rate constant for polymer elongation

$$\frac{d[E]}{dt} = k_n[A_1]([A_{tot}] - [A_1]) \quad [1]$$

$$\frac{d[A_1]}{dt} = -k_e[E][A_1]. \quad [2]$$

The relative concentration of nucleation seeds at the start of the experiment is described by the pseudoequilibrium constant $K = [A_{tot} - A_1]/[A_1]$. Optimization of the parameters led the values shown in the *SI Appendix*, Tables S1 and S2 and to the curves shown in Figs. 3*A* and 4*B*. These results show how dramatically ESCRT-II and CHMP6 accelerate nucleation of the CHMP4B polymer. With conditions held otherwise equal, the relative population of nucleation seeds $K = [A_{tot} - A_1]/[A_1]$ is 0.5–3 × 10^4-fold higher (with the range due to experimental variation) in the presence of ESCRT-II and CHMP6 than in their absence. In contrast, k_e changes by a factor of ∼3, and k_n barely changes at all. This simple model does not contain a detailed consideration of the available membrane surface sites, nor of the structural parameters of the polymer. Nevertheless, excellent fits to the data were obtained, and a satisfyingly clear account of the role of ESCRT-II and CHMP6 in activation via an increase the concentration of available seeds for nucleation.

Outgrowths of Snf7 (Yeast CHMP4) Form Flat Circular Domains Surrounding Invaginations. Given that flat spiral discs of CHMP4 have been observed previously (29, 30), we sought to determine whether CHMP4 would polymerize on the flat portion of the SLB at elevated concentrations. These experiments were not feasible with human CHMP4B because of its propensity to spontaneously aggregate at concentrations near the desired values. The yeast ortholog of CHMP4B is soluble at >5 μM, and we proceeded to image the growth of Snf7 domains at this concentration over 20 min (Fig. 5 *A* and *B* and Movies S2 and S3). Snf7 forms circular outgrowths as large as several micrometers in diameter, filling most of the space between invaginations. We also observed some nucleation on the flat part of the SLB, but estimated that growth initiated at invaginations accounted for ∼90% of the protein-covered surface area at the end of the 20-min incubation. Representative individual events of flat membrane nucleation were traced to kinetically compare them to invagination catalyzed initiation (Fig. 5 *C*–*E*). Initiation of the process was complete within a minute in the invaginations. In contrast, initiation on flat membranes showed a wide range of lag times, ranging up to the 30-min end point of the experiment (Fig. 5 and *SI Appendix*, Fig. S7*E*).

Superresolution Imaging of Snf7 Assembly and Outgrowth. To probe the nature of the assemblies in more detail, we imaged their assembly in real time using structured illumination microscopy (SIM) (31). At the higher resolution made possible by SIM, CHMP4 and Snf7 (Fig. 6 *A*–*D*) assemblies in invaginations are revealed as rings with radii of 250 nm. Comparison with the profiles shown in Fig. 1*A* indicates that annular zone occupied by CHMP4 and Snf7 corresponds to the most negatively curved part of the invaginations (Fig. 6*C*). We believe that the saturation of

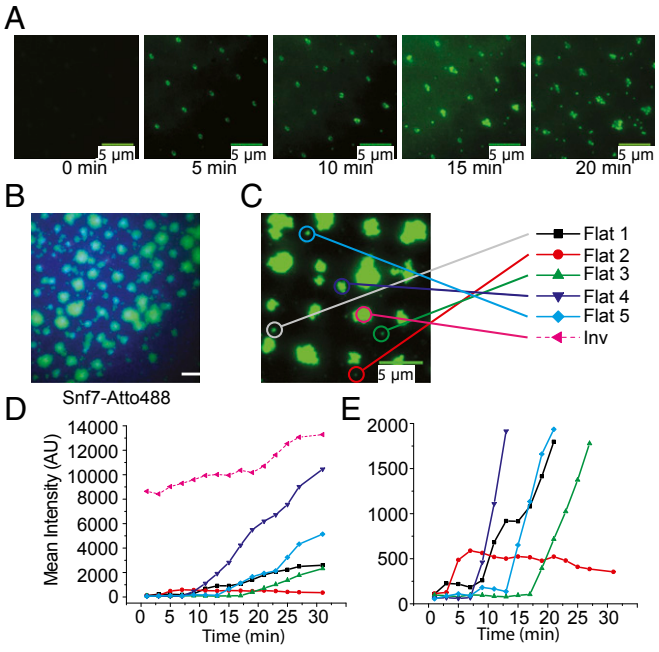

Fig. 5. Extended growth of Snf7 into the flat lipid bilayer is promoted by invagination nucleation. (*A*) Representative time lapse images of Snf7 outgrowth from 20-min incubation of 5 μM Snf7-Atto488. (Scale bars, 5 μm.) (*B*) TIRF image after 20-min incubation of 5 μM Snf7-Atto488. Large 2D fluorescent domains centered on invaginations are readily visible. Green, Atto488 fluorescence channel; blue, DiD fluorescence channel for lipids. (*C*) An example overgrowth image at the 20-min time point. Time-dependent intensity change was studied for individual nucleation events as indicated. Five representative events on the flat lipid membrane were compared with one event in an invagination. (*D*) Mean intensity change of each individual event. Intensity is already saturated within a minute in the case of invagination recruitment, whereas events on flat lipid bilayers are delayed. Circular ROI of 1 μm was used to calculate intensity. (*E*) The same plot of *D* is magnified to aid in comparing differential lag times of each nucleation event. The first steep increase indicates a nucleation event in which fluorescence puncta become readily visible on the flat side of lipid bilayers, and it is followed by continued growth except for Flat2. Single event traces were done as 2-min time lapse experiments.

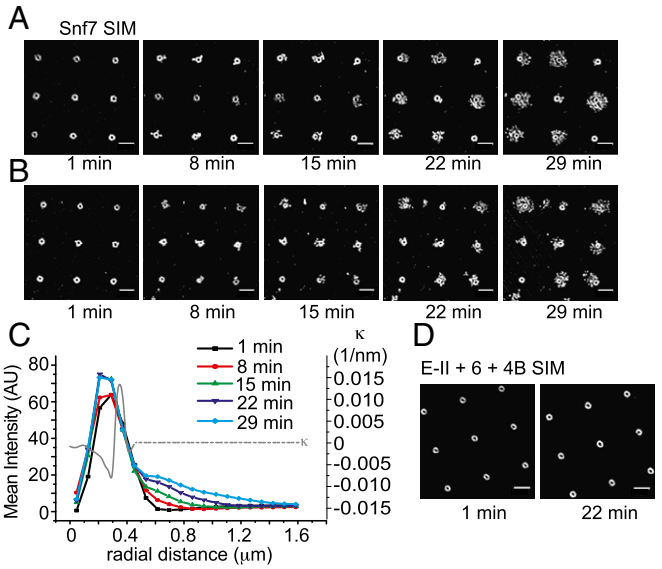

Fig. 6. Superresolution imaging of Snf7 assembly. (*A*) A set of representative time lapse SIM images of Snf7 outgrowth at 5 μM concentration. Snf7 is recruited as an annular structure around the edge of the invagination, which is followed by branched outward growth. (*B*) Another set of time lapse images of the same reaction. Relatively rare events (<5%) showed inward growth toward the centers. The center right and center bottom invaginations show examples of inward growth. (*C*) SIM intensity was radially averaged for each time point to quantify radial extension of Snf7 over time. The radial distance is defined as the distance from the center of each invagination. SIM clearly resolves the annular intensity peak for initial recruitment, followed by outward extension. Curvature calculation on a representative morphology as was done in Fig. 1 is overlaid. It clearly shows that the nucleation is catalyzed by the lipid bilayer of negative curvature region. The 3D geometry of the invagination is radially symmetric and the curvature calculated represents general geometric factor of invSLB. (*D*) SIM images of the recruitment of CHMP4B-Atto488 at ESCRT-II 100nM, CHMP6 200nM, CHMP4B 400nM. Circular recruitment around each lipid invagination is clear and it does not experience any further change over time. (Scale bars, 2 μm.)

the growth curves shown in Figs. 3*A* and 4*B* corresponds to occupancy of all of the available sites in this annular zone. The observed saturation is consistent with the concept that Snf7 and CHMP4 have a preference for binding negatively curved membranes.

We then went on to image the outgrowth of Snf7 at superresolution in real time. Snf7 fills the 250-nm radius annular zone within 1 min (Fig. 6 *A*–*C* and Movie S4). By 8 min, significant outward extensions are seen as far as 700 nm from the center of the invagination. The 700-nm radius places the farthest extension of the outgrowths about 350 nm past the edge of the curved rim. The extensions have the appearance of a meshwork of filaments. In a few instances, inward growth is seen, with the center of the annulus filled in over time. The inward growths represent fewer than 10% of the invaginations. Continuous outward growth of a filamentous meshwork is seen through 29 min, reaching as far at 1.35 μm from the invagination center, or nearly 1 μm from the rim. The imaged intensity in the time-lapse series was markedly affected by photobleaching. We imaged another example after 30-min unilluminated incubation (*SI Appendix*, Fig. S7), which revealed that all of the invaginations have extensive outgrowths. Even in the rare examples where the inside of the annulus is partly filled in, outward growth is observed.

Discussion

The recruitment of the ESCRTs to their sites of action has been extensively studied over the last decade and a half (1, 3). The roles of viral and host proteins and their ubiquitin modifications (32, 33) have been characterized in depth. Specific lipids such as PI(3)P are important in some settings, and negatively charged lipids are probably important in all cases (32). Given the unusual morphologies of the membranes with which ESCRTs function, it would seem that the shape of the membrane itself might be involved in recruitment. In particular, negative membrane curvature typically goes hand in hand with the sites of action of ESCRTs (6). However, is has not been feasible until now to directly test the extent to which membrane curvature controls ESCRT recruitment because the appropriate membrane substrates have not been available. Here, we tested one of the best characterized of all of the ESCRT subsystems, the ESCRT-II:CHMP6:CHMP4B module (23–27), in an in vitro assay for negative membrane curvature association. Our central finding is that when membrane invaginations are presented to CHMP4B in the context of a much larger surrounding of flat membrane, CHMP4B localizes strongly to the invaginations. From the SIM imaging, we further know that CHMP4B localizes to the most negatively curved part of the invaginations.

Here we established that ESCRT-III nucleation is accelerated by negative membrane curvature. The observed acceleration raises the question as to the structural basis of the effect. The N terminus of CHMP4B contains a stretch of hydrophobic residues that are important for membrane recruitment (34). Insertion of hydrophobic wedges typically favors binding to positively curved membranes (35), and it is hard to see how this property of CHMP4B would contribute to the negative curvature preference. The structure of the ESCRT-II:CHMP6 complex has a convex membrane binding site (24). It seems more likely that the ESCRT-III filament nucleus, consisting of several subunits, must also have a shape complementary to the negatively curved membrane.

By imaging the assembly of CHMP4B in real time, we sought to gain insight into the precise step in assembly that is promoted by negative curvature. We deduced that assembly is highly cooperative and that the availability of seeds for nucleation is the regulated step in polymerization. The presence of ESCRT-II and CHMP6 dramatically increased the nucleation of CHMP4. Kinetic competence is a critical test for in vitro models of complex cellular processes. Here, we observed that when activated by ESCRT-II and CHMP6, CHMP4B is recruited to the invagination over the course of 2 min, similar to the 3–5 min observed in live cell imaging of HIV-1 budding (11), satisfying this criterion. In contrast, neither the growth rate, nor the final size of the CHMP4 polymer, were greatly affected by the presence of ESCRT-II. In the current consensus model, one or a few copies of ESCRT-II and CHMP6 activate a similar number of CHMP4 molecules (23–27). In this model, additional copies of CHMP4 then add on to the polymer such that the stoichiometry of CHMP4 goes on to exceed that of the others. Our results provide a striking validation of the current model. Thus, it is not necessary that these three proteins form a complex simply to bind such membranes. Rather, that data show that the presence of ESCRT-II and CHMP6 converts CHMP4B into a far more effective seed for subsequent polymerization. Thus, both negative membrane curvature and the presence of upstream activating proteins act by increasing nucleation.

At the submicromolar concentrations used for most of the experiments in the study, ESCRT localization was confined to the membrane invaginations. At low micromolar concentrations, the yeast CHMP4 ortholog Snf7 also began polymerizing in the invaginations. Nucleation events were also observed elsewhere on the flat portion of the SLB, but these appeared at later times. Invagination-catalyzed nucleation was complete within one minute, while the initiation process on flat membranes were delayed up to the end-point of the experiment at 30 min. The spectrum of lag times appeared to be randomly distributed. The broad lag time distribution suggests that, without geometric assistance, nucleation is the rate-limiting step for assembly formation.

Over the course of several minutes, Snf7 assemblies that nucleated in the invaginations proceeded to grow into circular domains that expanded onto the flat SLB. SIM imaging showed that these domains consist of a meshwork of filaments that extend outward from the central annulus. Thus, nucleation events that occurred on the negatively curved part of the membrane were capable of spawning outgrowths onto the flat surroundings.

A key conclusion of this study is that ESCRT-III complexes nucleate rapidly at the zone of negative curvature in membrane invaginations of physiological dimensions. This finding provides a biophysical mechanism for the observation that ESCRT-III is recruited in a short burst at the very end of HIV-1 Gag assembly at the plasma membrane (10). The delayed recruitment of ESCRT-III in turn explains how ESCRT-mediated membrane scission is delayed until formation of the immature Gag lattice is close to completion. It might also help explain the timing of the second burst of ESCRT-III assembly close to the abscission site in cytokinesis (36).

Another second important conclusion is that once nucleated, ESCRT-III assemblies are capable of polymerizing outward to flat surfaces. In fact, this is the preferred direction. Inward polymerization was rarely seen. Firm conclusions about the scission mechanism cannot be drawn from the invSLB system because the membrane is held in place rigidly. The results do, however, seem to be consistent with the finding that in EM images of ESCRT-III assemblies surrounding HIV-1 Gag budding sites, the filaments seem to spiral outward from the rim of budding site, not inward (37). The outward growth direction may be hard to reconcile with the popular dome model for membrane scission in which a close-packed hemisphere of ESCRTs is formed that brings the walls of the membrane neck close enough for fusion (38).

Materials and Methods

Nanocurvature was fabricated on the coverslip with a focused ion beam (FIB; FEI Quanta). The resulting geometry was measured by AFM (Asylum Research MFP-3D). The lipid mixture POPC:POPS:PI(3)P:DiD = 82:15:3:0.005 (except where noted otherwise) was used to form 100-nm liposomes, which were in turn incubated with piranha-cleaned glass to form SLBs. ESCRT proteins were purified from an *Escherichia coli* expression system and labeled with Atto-488. TIRF (total internal reflection fluorescence) microscopy was performed with a Nikon Ti-E–based microscope (Nikon). SIM was performed using an ELYRA SR.1 Superresolution Microscopy (Zeiss) instrument.

ACKNOWLEDGMENTS. We thank Peidong Yang and Chong Liu for AFM measurements; Bei Yang, Qingtao Shen, Gerhard Hummer, and Johannes Schöneberg for advice and discussions; the Berkeley Marvell nanofabrication laboratory and Biomolecular Nanotechnology Center for use of nanofabrication instruments; and the Berkeley CNR Biological Imaging Facility for access to and assistance with SIM microscopy. This work was supported by National Institute of Allergy and Infectious Diseases of the National Institutes of Health Grant R01AI112442. Partial support was provided by the National Cancer Institute of the National Institutes of Health under Award no. U01CA202241(to J.T.G.).

1. Hurley JH, Hanson PI (2010) Membrane budding and scission by the ESCRT machinery: It's all in the neck. *Nat Rev Mol Cell Biol* 11(8):556–566.
2. McCullough J, Colf LA, Sundquist WI (2013) Membrane fission reactions of the mammalian ESCRT pathway. *Annu Rev Biochem* 82(1):663–692.
3. Votteler J, Sundquist WI (2013) Virus budding and the ESCRT pathway. *Cell Host Microbe* 14(3):232–241.
4. Agromayor M, Martin-Serrano J (2013) Knowing when to cut and run: Mechanisms that control cytokinetic abscission. *Trends Cell Biol* 23(9):433–441.
5. Hanson PI, Cashikar A (2012) Multivesicular body morphogenesis. *Annu Rev Cell Dev Biol* 28(28):337–362.
6. Hurley JH (2015) ESCRTs are everywhere. *EMBO J* 34(19):2398–2407.
7. Morita E, et al. (2011) ESCRT-III protein requirements for HIV-1 budding. *Cell Host Microbe* 9(3):235–242.
8. Meng B, Ip NCY, Prestwood LJ, Abbink TEM, Lever AML (2015) Evidence that the endosomal sorting complex required for transport-II (ESCRT-II) is required for efficient human immunodeficiency virus-1 (HIV-1) production. *Retrovirology* 12:72.
9. Carlson LA, Hurley JH (2012) In vitro reconstitution of the ordered assembly of the endosomal sorting complex required for transport at membrane-bound HIV-1 Gag clusters. *Proc Natl Acad Sci USA* 109(42):16928–16933.
10. Bleck M, et al. (2014) Temporal and spatial organization of ESCRT protein recruitment during HIV-1 budding. *Proc Natl Acad Sci USA* 111(33):12211–12216.
11. Jouvenet N, Zhadina M, Bieniasz PD, Simon SM (2011) Dynamics of ESCRT protein recruitment during retroviral assembly. *Nat Cell Biol* 13(4):394–401.
12. Van Engelenburg SB, et al. (2014) Distribution of ESCRT machinery at HIV assembly sites reveals virus scaffolding of ESCRT subunits. *Science* 343(6171):653–656.
13. Prescher J, et al. (2015) Super-resolution imaging of ESCRT-proteins at HIV-1 assembly sites. *PLoS Pathol* 11(2):e1004677.
14. Kräusslich HG, Fäcke M, Heuser AM, Konvalinka J, Zentgraf H (1995) The spacer peptide between human immunodeficiency virus capsid and nucleocapsid proteins is essential for ordered assembly and viral infectivity. *J Virol* 69(6):3407–3419.
15. von Schwedler UK, et al. (2003) The protein network of HIV budding. *Cell* 114(6): 701–713.
16. Carlson LA, et al. (2008) Three-dimensional analysis of budding sites and released virus suggests a revised model for HIV-1 morphogenesis. *Cell Host Microbe* 4(6):592–599.
17. Mercenne G, Alam SL, Arii J, Lalonde MS, Sundquist WI (2015) Angiomotin functions in HIV-1 assembly and budding. *eLife* 4:4.
18. McMahon HT, Gallop JL (2005) Membrane curvature and mechanisms of dynamic cell membrane remodelling. *Nature* 438(7068):590–596.
19. Chan Y-HM, Boxer SG (2007) Model membrane systems and their applications. *Curr Opin Chem Biol* 11(6):581–587.
20. Samiee KT, Moran-Mirabal JM, Cheung YK, Craighead HG (2006) Zero mode waveguides for single-molecule spectroscopy on lipid membranes. *Biophys J* 90(9):3288–3299.
21. Frost A, Unger VM, De Camilli P (2009) The BAR domain superfamily: Membrane-molding macromolecules. *Cell* 137(2):191–196.
22. van Weering JRT, et al. (2012) Molecular basis for SNX-BAR-mediated assembly of distinct endosomal sorting tubules. *EMBO J* 31(23):4466–4480.
23. Saksena S, Wahlman J, Teis D, Johnson AE, Emr SD (2009) Functional reconstitution of ESCRT-III assembly and disassembly. *Cell* 136(1):97–109.
24. Im YJ, Wollert T, Boura E, Hurley JH (2009) Structure and function of the ESCRT-II-III interface in multivesicular body biogenesis. *Dev Cell* 17(2):234–243.
25. Teis D, Saksena S, Judson BL, Emr SD (2010) ESCRT-II coordinates the assembly of ESCRT-III filaments for cargo sorting and multivesicular body vesicle formation. *EMBO J* 29(5):871–883.
26. Fyfe I, Schuh AL, Edwardson JM, Audhya A (2011) Association of the endosomal sorting complex ESCRT-II with the Vps20 subunit of ESCRT-III generates a curvature-sensitive complex capable of nucleating ESCRT-III filaments. *J Biol Chem* 286(39): 34262–34270.
27. Henne WM, Buchkovich NJ, Zhao Y, Emr SD (2012) The endosomal sorting complex ESCRT-II mediates the assembly and architecture of ESCRT-III helices. *Cell* 151(2): 356–371.
28. Ruschak AM, Miranker AD (2007) Fiber-dependent amyloid formation as catalysis of an existing reaction pathway. *Proc Natl Acad Sci USA* 104(30):12341–12346.
29. Hanson PI, Roth R, Lin Y, Heuser JE (2008) Plasma membrane deformation by circular arrays of ESCRT-III protein filaments. *J Cell Biol* 180(2):389–402.
30. Shen QT, et al. (2014) Structural analysis and modeling reveals new mechanisms governing ESCRT-III spiral filament assembly. *J Cell Biol* 206(6):763–777.
31. Gustafsson MGL (2000) Surpassing the lateral resolution limit by a factor of two using structured illumination microscopy. *J Microsc* 198(Pt 2):82–87.
32. Raiborg C, Stenmark H (2009) The ESCRT machinery in endosomal sorting of ubiquitylated membrane proteins. *Nature* 458(7237):445–452.
33. Shields SB, Piper RC (2011) How ubiquitin functions with ESCRTs. *Traffic* 12(10): 1306–1317.
34. Buchkovich NJ, Henne WM, Tang S, Emr SD (2013) Essential N-terminal insertion motif anchors the ESCRT-III filament during MVB vesicle formation. *Dev Cell* 27(2):201–214.
35. Campelo F, McMahon HT, Kozlov MM (2008) The hydrophobic insertion mechanism of membrane curvature generation by proteins. *Biophys J* 95(5):2325–2339.
36. Elia N, Sougrat R, Spurlin TA, Hurley JH, Lippincott-Schwartz J (2011) Dynamics of endosomal sorting complex required for transport (ESCRT) machinery during cytokinesis and its role in abscission. *Proc Natl Acad Sci USA* 108(12):4846–4851.
37. Cashikar AG, et al. (2014) Structure of cellular ESCRT-III spirals and their relationship to HIV budding. *eLife* 3:02184.
38. Fabrikant G, et al. (2009) Computational model of membrane fission catalyzed by ESCRT-III. *PLOS Comput Biol* 5(11):e1000575.

Supporting Information

Lee et al. 10.1073/pnas.1518765113

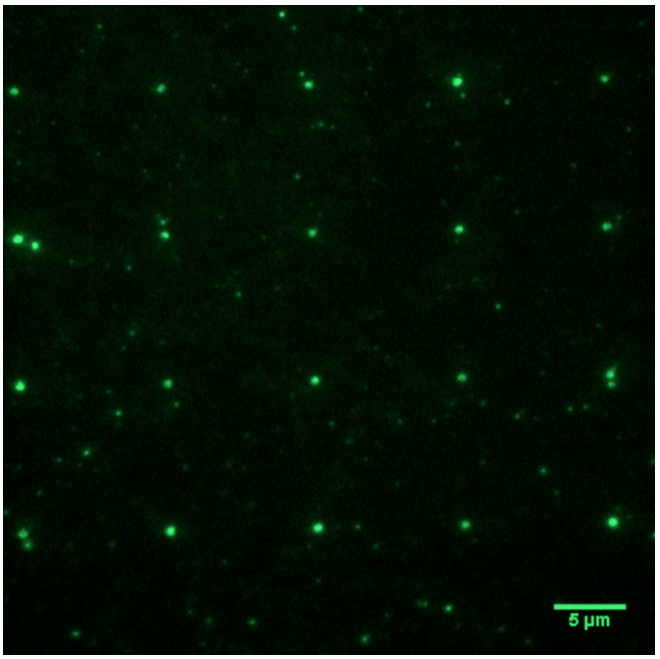

Movie S1. Time lapse movie of CHMP4B recruitment to invaginations. TIRF fluorescence time lapse images acquired every 1 min played at four frames per second. The Atto488 channel is the only signal shown in the movie. The regular spacing of the invaginations is clearly visible from the protein recruitment. The intensity decay at later times is due to photobleaching. The proteins incubated were 40 nM CHMP4B-Atto488, 100 nM ESCRT-II, and 200 nM CHMP6.

Movie S1

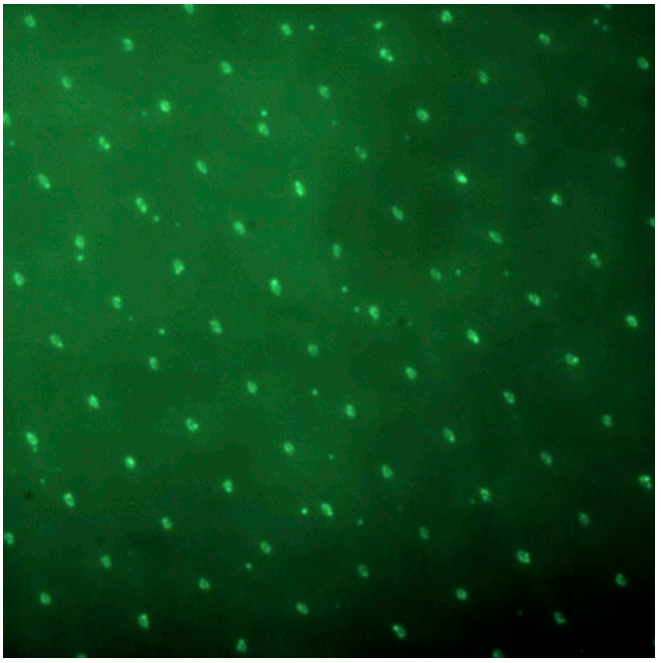

Movie S2. Time lapse movie of Snf7 overgrowth 1. TIRF fluorescence time lapse images were acquired every 15 s played at four frames per second. Green, Atto488 channel, the only signal shown in the movie. The proteins incubated were 5 μM Snf7-Atto488 and 200 nM Vps20ΔC.

Movie S2

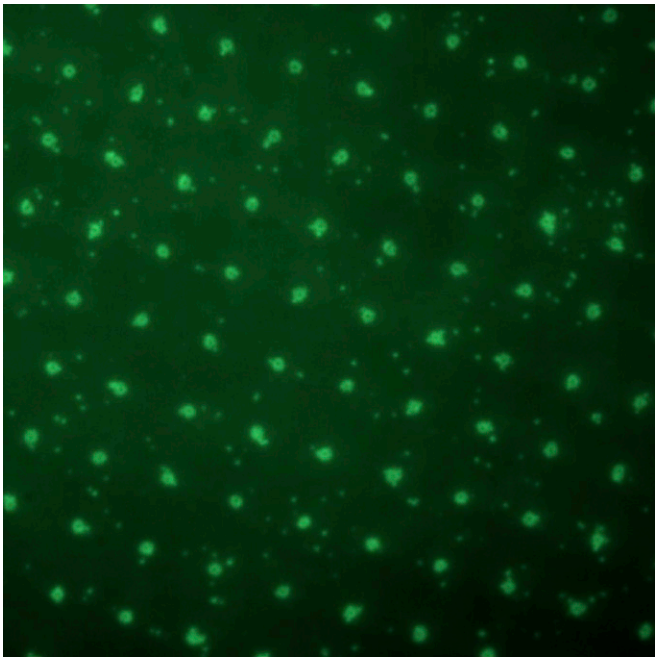

Movie S3. Time lapse movie of Snf7 overgrowth 2. A second movie recorded under the same conditions as Movie S2.

Movie S3

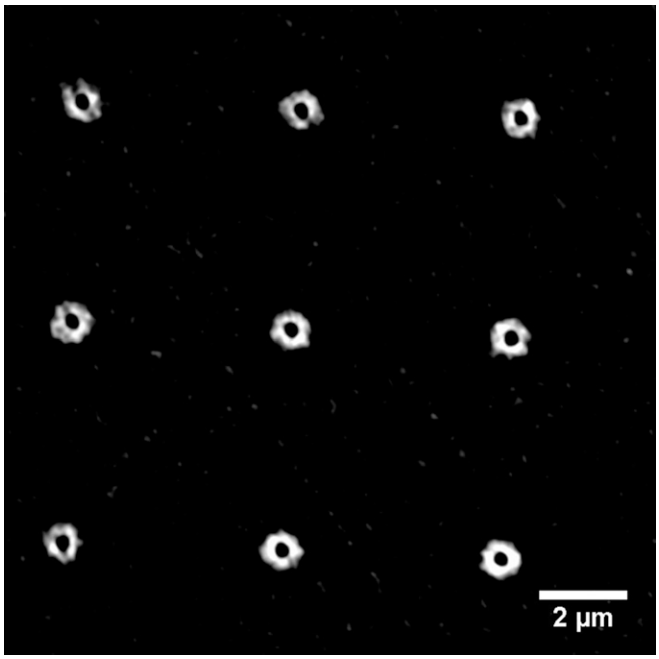

Movie S4. Time lapse structured illumination movie of Snf7 overgrowth. SIM time lapse images were acquired and reconstructed every 7 min starting at 1 min from a 5 μM Snf7-Atto488 sample. The video is played at one frame per second (420× real time). White SIM intensity is from the Atto488 channel.

Movie S4

Other Supporting Information Files

SI Appendix (PDF)

Materials and Methods

Nanofabrication and characterization of glass substrates

Glass coverslips (25 mm diameter, 0.17 mm thickness, No. 1.5; Harvard Apparatus) were cleaned by sonication in isopropanol/water (1:1 volume) for 30 min, rinsed with a stream of ultrapure water, cleaned with piranha solution (conc. H_2SO_4/H2O2 (30%), 3:1 volume) for 5 min at room temperature, rinsed with a stream of ultrapure water, and dried with a flow of nitrogen. A thin film of chromium (6 nm) as a conductive layer was deposited on the cleaned coverslip by an e-beam metal evaporator (Edwards EB3) with 0.1-0.5 nm/sec deposition rate. Nanocurvature was fabricated on the coverslip with a focused ion beam (FIB; FEI Quanta) operated at 30 kV and 1 nA using a cylindrical milling shape of 100 nm in diameter and 100 nm in depth. The chromium film was removed by immersing the coverslip in concentrated HCl aq. and touching the surface with an aluminum wire. The coverslip was rinsed with deionized water and dried with a flow of nitrogen. The resulting geometry was measured by atomic force microscopy (AFM; Asylum Research MFP-3D) at a tapping mode with 335 kHz frequency.

invSLB formation

A lipid stock solution in chloroform (Avanti polar lipids, Alabama, US) was mixed to yield the composition of interest. POPC (1-palmitoyl-2-oleoyl-sn-glycero-3-phosphocholine) and POPS (1-palmitoyl-2-oleoyl-sn-glycero-3-phospho-L-serine) were from Avanti polar lipids (Alabama, USA). PI(3)P (Dipalmitoyl phosphatidylinositol 3-phosphate) was from Echelon bioscience (Utah, USA). DiD was from Life Technologies (CA, USA). The composition used in all experiments was POPC:POPS:PI(3)P:DiD = 82:15:3:0.005 except where specified otherwise. For quantitation of PS distribution, the labeled lipid TopFluor-PS (1-palmitoyl-2-(dipyrrometheneboron difluoride)undecanoyl-sn-glycero-3-phospho-L-serine; Avanti Polar Lipids, Alabama, US) was used. The lipid mixtures were dried on a piranha etched round bottom flask under nitrogen, followed by overnight incubation in a vacuum chamber. Milli-Q filtered water (EMD Millipore, MA, USA) was added to reach 2 mg/ml total lipid concentration. Freezing and thawing was repeated three times to hydrate lipids into water. A hand held extruder (Avanti polar lipids, Alabama, US) was used to extrude lipids through a 100 nm sized filter (Whatman, PA, USA) nine times. The extruder was cleaned by 30 min sonication in 1%

Hellmanex (Hellma analytics) followed by another 30 min in water before use. Liposomes were kept at 4 ˚C and were used within one day.

Nanofabricated glass substrates were cleaned with piranha solution (concentrated sulfuric acid: hydrogen peroxide = 3:1) before each use. Clean substrates were assembled into the Attofluor cell chambers (Life technologies, CA, USA). Liposome solutions were mixed with 1x PBS solution containing 5 mM $MgCl_2$ at a 1:1 ratio, and the solution was incubated on top of glass substrates for one hour. The samples were washed by exchanging buffer five times without exposing the lipid membrane surface to air, and the SLB was used immediately after preparation. The solution phase buffer 150mM NaCl, 50mM Tris, pH 7.4 was used throughout unless specified otherwise. Membrane fluidity was checked before starting each experiment. Nanofabricated glass substrates were reused up to three times by thoroughly washing with 1% detergent solution and isopropyl alcohol. Repeated reuse of substrate more than five times resulted in the formation of immobile bilayers, and therefore the substrates were discarded after three uses. We found our supported lipid bilayer system becomes immobile after ~1 hour from its formation as detected by FRAP experiments, suggesting instability of the highly charged supported lipid bilayer system over longer time scales. The bilayer was stable without change of membrane properties within the time window of all experiments carried out in this report.

For the His_6-tethered control experiments shown in Figure 2, 1% Ni-DOGS lipids replaced an equivalent amount of POPC. After the initial formation of the SLB, the bilayer was incubated with 100 mM NiCl for 5 min, washed, then incubated with 10nM His_6-tagged proteins for 30 min. Ni-DOGS (1,2-dioleoyl-sn-glycero-3-[(N-(5-amino-1-carboxypentyl) iminodiacetic acid)succinyl]) was from Avanti Polar Lipids.

Protein expression and purification

Protein expression and purification was carried out as previously described (1). Briefly, the human ESCRT-II complex was expressed in *E. coli* as a TEV protease-cleavable His_6 fusion protein (2) and labeled on native lysine residues using Atto488 NHS ester (Sigma-Aldrich, MO, USA). Human and yeast ESCRT-III subunits were expressed and purified as previously described (1), and labeled with Atto488 maleimide (Sigma-Aldrich) on engineered unique cysteine residues. The SNX1 BAR domain and 88-522 construct were purified as previously described (3). Briefly, they were expressed as MBP fusion proteins in *E. Coli* and the tags were

removed by TEV protease cleavage of the linker region. Tag fragments were removed by Ni-NTA beads followed by Superdex 200 (GE Healthcare) purification. Purified proteins were fluorescently labeled by incubating with a 10-fold molar excess of Alexa488 NHS ester for non-specific labeling at 4 ˚C overnight. Excess dye was removed with a HiTrap desalting column (GE Healthcare). The labeling ratio was in the range of 0.5-1.0 dye per protein.

TIRF imaging

TIRF microscopy was performed with a Nikon Ti-E based microscope (Nikon, Tokyo, Japan) with an ASI automatic stage (Applied Scientific Instrumentation, OR, USA). The excitation laser source was an OPSL smart laser module (Coherent, CA, USA) coupled to the microscope by optical fibers of an ILE merge module (Spectra Physics, CA, USA) with fixed fiber alignment. Excitation wavelengths of 488, 532, 640 nm were used. Laser intensity was voltage controlled from the controlling computer. Chroma optical filter sets (Chroma technology, VT, USA) of excitation dichroic, excitation wavelength filter, emission wavelength filters for each TIRF wavelength were used. A 100X TIRF NA1.49 oil objective (Nikon) was used with 1.5x emission path magnification. An Andor Ixon Ultra EMCCD camera with 512 x 512 pixels (Andor Technology, Belfast, UK) was used for image acquisition without electron multiplication gain. An emission filter wheel (Sutter Instrument, CA, USA) with emission bandwidth filters was used for noise elimination. The whole setup was installed on a gas floated vibration isolation table (TMC, CA, USA). All devices were automatically controlled from the controlling computer by Micro manager, an ImageJ based software (https://www.micro-manager.org/).

Laser power used was ~12mW (488 nm), ~3mW (532 nm), ~6mW (640 nm) for each wavelength excitation as measured right before the objective. The TIRF angle was adjusted to ensure surface-specific excitation. The image acquisition time was 100 ms for all data shown unless specified otherwise. Multi-color imaging was always performed from higher to lower wavelength excitation. Sample chambers were firmly held by the stage adaptor to minimize mechanical drift during time lapse imaging. A perfect focus system (Nikon) prevented loss of focus during the time lapse imaging. An oxygen scavenger system (4) consisting of glucose, glucose oxidase and catalase (all from Sigma-Aldrich) was added right before imaging to minimize photobleaching.

The slightly higher DiD intensity observed by TIRF near the invaginations can be

accounted for by the higher area density of fluorophores as projected onto a plane. Given a half ellipsoidal shape with radius of r=200nm and depth d=100nm, the surface area of an invagination is 1.38 of the corresponding flat region, from $2\pi r \left(\frac{(r*r)^{1.6}+2(r*d)^{1.6}}{3}\right)^{1/1.6} / \pi r^2 = 1.38$. We observe that the DiD emission intensity in invaginations is ~1.5-fold greater than the surrounding flat membrane (Fig. 1D) consistent with this topography.

SIM imaging

Structured illumination microscopy (SIM) was performed using an ELYRA SR.1 Superresolution Microscopy (Zeiss, Oberkochen, Germany) instrument. A 100x oil objective was used with 1.6x final magnification. A sCMOS camera was used to collect the signal for the SIM mode. 488nm laser excitation SIM mode data acquisition was performed for each time point after initiating the reaction. The Z-position was manually focused for each acquisition to use as a z-stack center. Images were acquired as z-stacks of a 0.1 µm step spanning 1 µm, with the focal point as the z-scan center. Images were acquired from 3 different grating illumination patterns that are 120 µm from each other with a 200 ms exposure time to complete one set of full SIM acquisition. Sets of images were later constructed into complete images by the automated SIM analysis of the software ZEN white (Zeiss).

Data analysis

ImageJ (http://imagej.nih.gov/ij/) was used for image analysis. For quantification of total intensity in each invagination, n > 60 invaginations in at least six different images from different positions were analyzed. A fixed size circular region of interest was used for the same set of data. For kinetic analysis, same strategy was used for the each image across the entire time window. For time lapse studies, n=30 invaginations from six image stacks from different positions were analyzed. Radial analysis of Figure 7C was performed as an automated image analysis in Matlab R2014b (Mathworks, MA, USA). Center positions for invaginations (n=67) were manually determined by examining images to generate lists of Cartesian coordinates. Intensity values and distances of pixels around the centers were collected and binned by distance. Total intensity summation was divided by the number of pixels in the bin to obtain the final

average intensity value for each distance bin. Each data point of Figure 7C was plotted at the mean distance of each distance bin in x axis.

Deterministic nucleation growth model

The set of ordinary differential equations (ODE) was solved numerically using the ode45 function in Matlab R2014b (Mathworks, MA, USA). ODEs describing the elementary chemical reactions were adapted from a model previously applied to the nucleation and growth of amyloid fibers (5). The nucleation step generates the polymer elongation ends, E. Multimer-dependent nucleation is of order *m* with respect to the non-monomer concentration.

$$\frac{d[E]}{dt} = k_n[A_1]^n([A_{tot}] - [A_1])^m$$

Here, [E] denotes concentration of elongation ends, $[A_1]$ is monomer concentration, $[A_{tot}]$ is total protein concentration, and k_n is the rate constant of nucleation reaction. We used $n = 1$, however, varying n from 0 to 2 did not alter the general trends of the sigmoidal growth with variations in absolute values. We found that $m = 1$, which is the same order as the original model we adapted from, provided good fits to the data. Polymer elongation takes the form of reaction between elongation ends and monomers:

$$\frac{d[A_1]}{dt} = -k_e[E][A_1]$$

Here, k_e is the kinetic constant of elongation. The concentration of polymer on the membrane, [Multimer] = $[A_{tot}]$-$[A_1]$, is equivalent to the fluorescence intensity in our experiments. The initial condition was set accordingly for each constant $K = ([\mathrm{A_{tot}}] - [A_1])/[A_1]$, $[\mathrm{A_1}]_0 = [\mathrm{A_{tot}}]/(1 + \mathrm{K})$, and $[\mathrm{E}]_0 = 0$. $[A_{tot}]$ was determined from experimental values. Nonlinear parameter optimization was performed by nlinfit function in Matlab as a simultaneous three parameter (K, k_n, k_e) optimization problem with respect to the experimental data. $([\mathrm{A_{tot}}] - [A_1])$ was treated as the fluorescence readout of multimer formation. The background signal was subtracted beforehand.

Supplementary Figure legends

Figure S1. Characterization of invaginated supported lipid bilayers (invSLBs).
(A) Sample line profiles of the nano-fabricated glass surface. The geometries shown are actual morphologies measured by atomic force microscopy. Each panel a, b, c was obtained from a scan along one of lines shown in (B). (B) AFM measurements on FIB fabricated substrates. The upper orange colored lines indicate the scans shown in (A) and the yellow colored box indicates the region shown in the surface plot in Figure 1C.

Figure S2. PS is uniformly distributed on invSLBs.
Sample TIRF image and line profile of POPC:POPS:PI(3)P:DiD:TopFluor-PS 82:15:3:0.005:0.005 on invSLB.

Figure S3. Control experiments for invagination specific recruitment and line intensity profiles of ubiquitin, BAR and SNX1 88-522.
(A) TIRF image after 20 min incubation of 400 nM ubiquitin-Atto488 (no His_6 tag) as a control for non-specific recruitment. Atto488 fluorescence contrast was scaled exactly the same as in Figure 2A for direct comparison. (B) TIRF image after 20 min incubation of 100 nM BSA-Cy3. Blue indicates membrane-tethered His_6-ubiquitin-Cy5 as a control for membrane binding induced recruitment. Scale bars are 5 μm. (C) TIRF fluorescence image after 20 min incubation of 400 nM BAR-Alexa488. (D) TIRF fluorescence image after 20 min incubation of 400 nM SNX1 88-522-Alexa488. (C) and (D) were scaled the same as (A) for direct comparison. Representative intensity profiles (yellow lines) from the 400 nM incubation of (E) Ubiquitin-Atto488, (F) BAR-Alexa488 and (G) SNX1 88-522-Alexa488 with PC, PS, and PI3P. Intensity values are shown as raw values. Scale bars are 5μm.

Figure S4. Time lapse images for the sigmoidal kinetics of CHMP4B recruitment to invaginations.
Representative time lapse images for the (A) 40nM, and (B) 4nM CHMP4B-Atto488 experiments of the Figure 3. Scale bars are 5 μm.

Figure S5. Time lapse images for ESCRT-II and CHMP6 promoted CHMP4B nucleation.
Representative time lapse images of the (A) CHMP6+ CHMP4B-Atto488 and (B) CHMP4B-Atto488 experiments of the Figure 4. Further images are shown in Figure S4.Scale bars are 5 μm.

Figure S6. Single invagination analysis of lag time distribution.
Lag times of individual invagination assemblies were calculated from the data shown in Figure 4B. Lag times were quantified by fitting each individual trace with a general sigmoidal equation $y = y_0 + y_m(1/\exp(\frac{t_{lag}-x}{r}))$ where y_0 and y_m denote offset and maximum y values each. t_{lag} is the lag time and r is an arbitrary rate constant. Relatively narrow distribution of lag time compared to the difference between averages at different conditions suggests the event within an invatination is from sufficiently large number of molecules that the average behavior over all invaginations can be well approximated by single invagination kinetics. We attribute the slightly greater variation in the case of ESCRT-II, CHMP6 and CHMP4B to the very short lag time, resulting in the truncation of earliest part of the sigmoidal kinetics in some cases.

Figure S7. Lag time distribution for nucleation on flat and invaginated membranes.
Lag times of individual assembly initiation were calculated from the experiment shown in Figure 5C. N=35 initiation events on flat membrane region were examined manually to study intensity traces similar to Figure 5E. Lag times were defined and quantified by manually determining the very first time point of steep intensity increase. Quantified intensity histogram is shown as green bars. Invagination assisted initiation was already complete for all invaginations within a minute of incubation as indicated by a gray bar. Lag times are widely distributed within 30 min time window of observation suggesting stochastic nature of the events on flat lipid bilayers while invagination geometry dramatically catalyzes the initiation of overgrowth.

Figure S8. SIM images after 30 min incubation without photo-bleaching.
Representative SIM images after 30 min incubation in the dark.

References

1. Carlson LA & Hurley JH (2012) In Vitro Reconstitution of the Ordered Assembly of the ESCRT Machinery at Membrane-Bound HIV-1 Gag Clusters. *Proc Natl Acad Sci U S A* 109:16928-16933.
2. Im YJ & Hurley JH (2008) Integrated structural model and membrane targeting mechanism of the human ESCRT-II complex. *Dev Cell* 14:902-913.
3. van Weering JRT*, et al.* (2012) Molecular basis for SNX-BAR-mediated assembly of distinct endosomal sorting tubules. *EMBO J.* 31(23):4466-4480.
4. Rasnik I, McKinney SA, & Ha T (2006) Nonblinking and long-lasting single-molecule fluorescence imaging. *Nat Meth* 3(11):891-893.
5. Ruschak AM & Miranker AD (2007) Fiber-dependent amyloid formation as catalysis of an existing reaction pathway. *Proceedings of the National Academy of Sciences* 104(30):12341-12346.

A

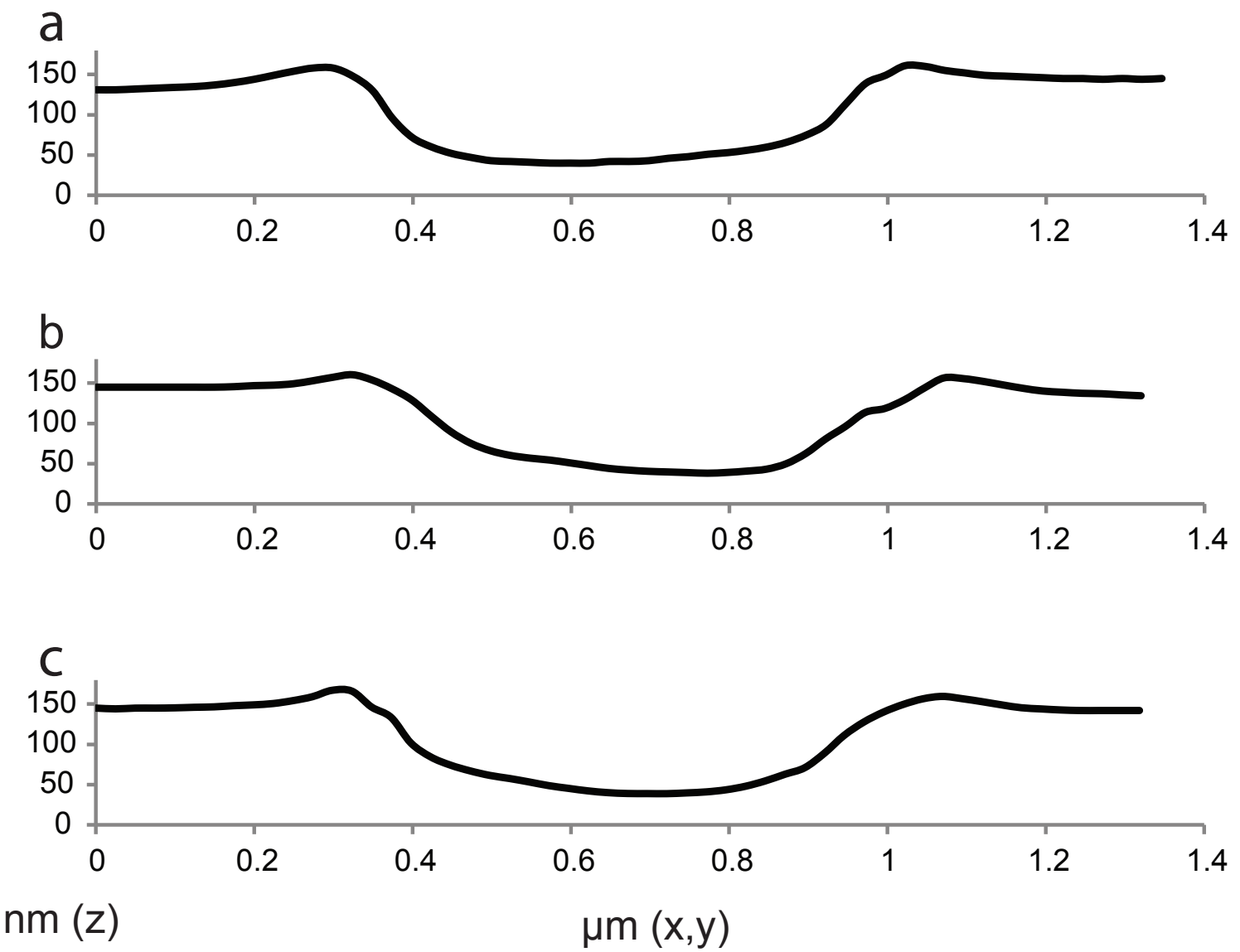
a
150
100
50
0
0
0.2
0.4
0.6
0.8
1
1.2
1.4
b
150
100
50
0
0
0.2
0.4
0.6
0.8
1
1.2
1.4
c
150
100
50
0
0
0.2
0.4
0.6
0.8
1
1.2
1.4
nm (z)
µm (x,y)

B

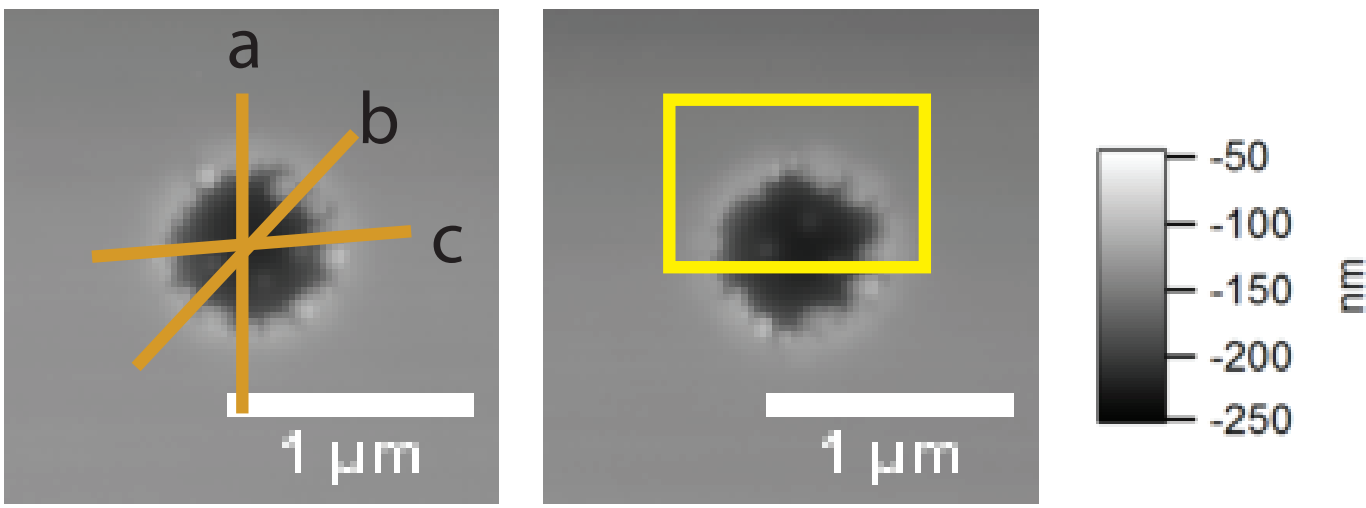
a
b
c
1 µm
1 µm
-50
-100
-150
-200
-250
nm

Figure S1

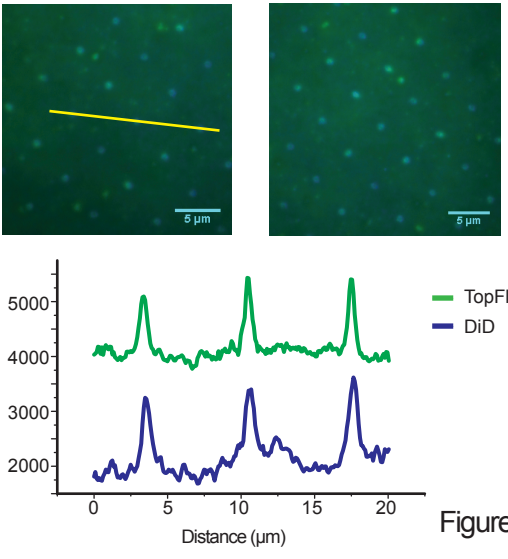
5 µm
5 µm
Intensity (AU)
5000
4000
3000
2000
0
5
10
15
20
Distance (µm)
TopFluor-PS
DiD

Figure S2

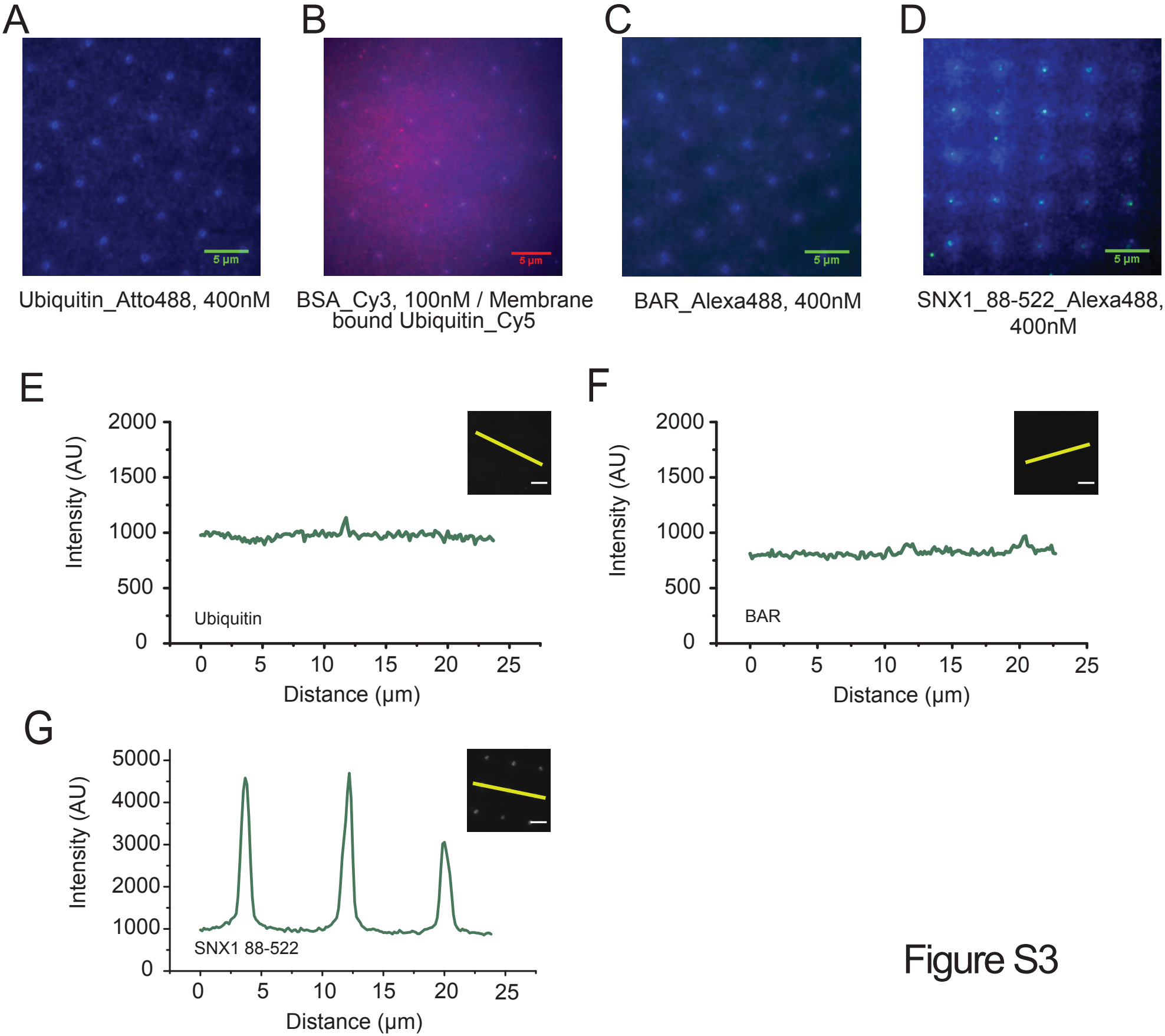
A
B
C
D
5 µm
Ubiquitin_Atto488, 400nM
BSA_Cy3, 100nM / Membrane bound Ubiquitin_Cy5
BAR_Alexa488, 400nM
SNX1_88-522_Alexa488, 400nM
E
F
G
Intensity (AU)
Distance (µm)
Ubiquitin
BAR
SNX1 88-522
0
500
1000
1500
2000
2000
3000
4000
5000
0
5
10
15
20
25

Figure S3

A

40 nM

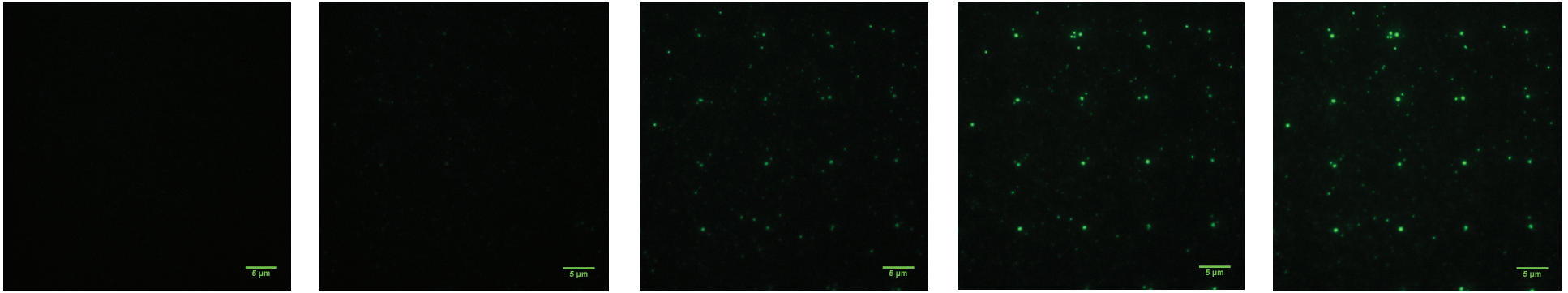

0 min 2 min 4 min 6 min 8 min

B

4 nM

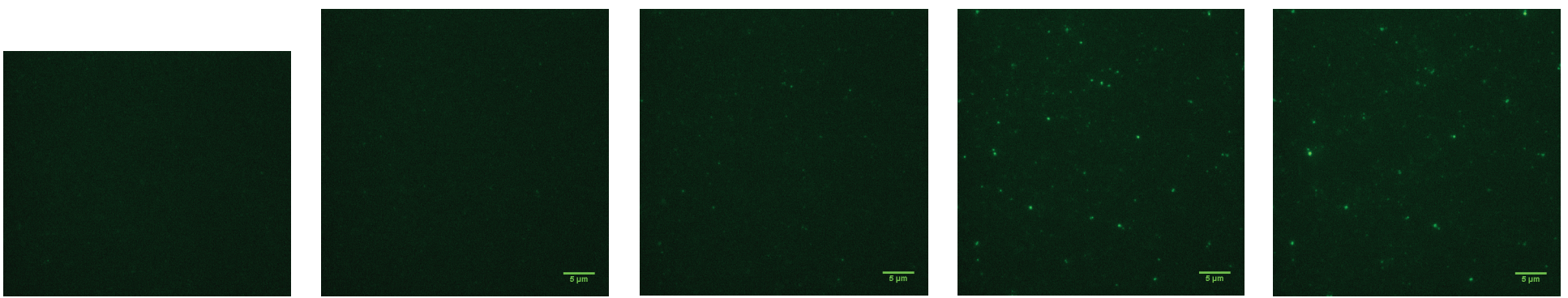

0 min 4 min 8 min 12 min 16 min

Figure S4

A

CHMP6 + CHMP4B

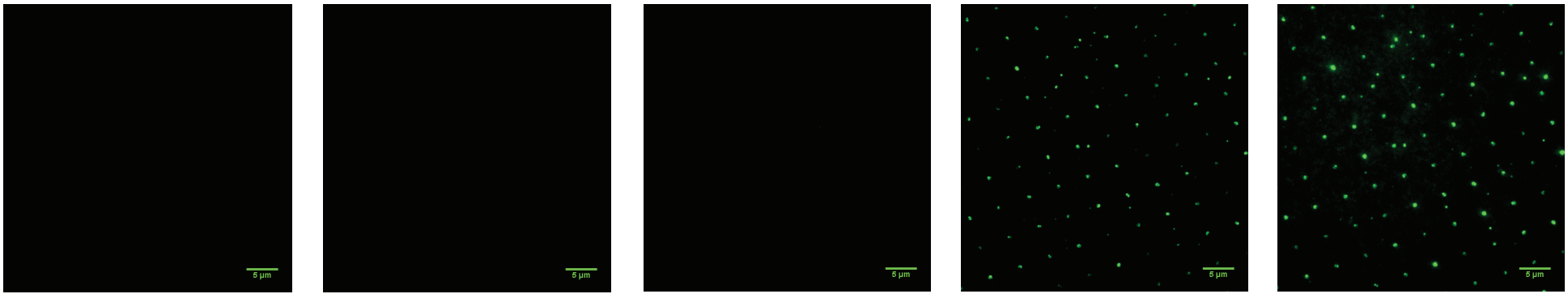

0 min 3 min 6 min 9 min 12 min

B

CHMP4B

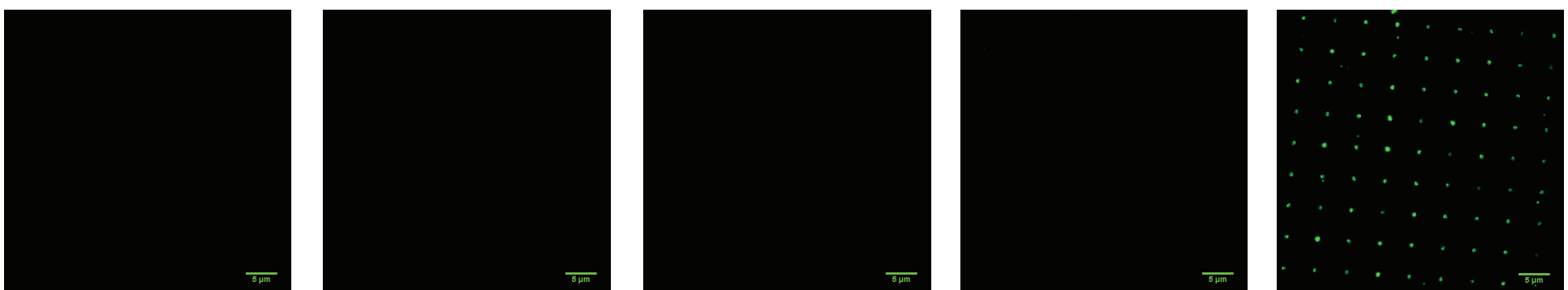

0 min 4 min 8 min 12 min 16 min

Figure S5

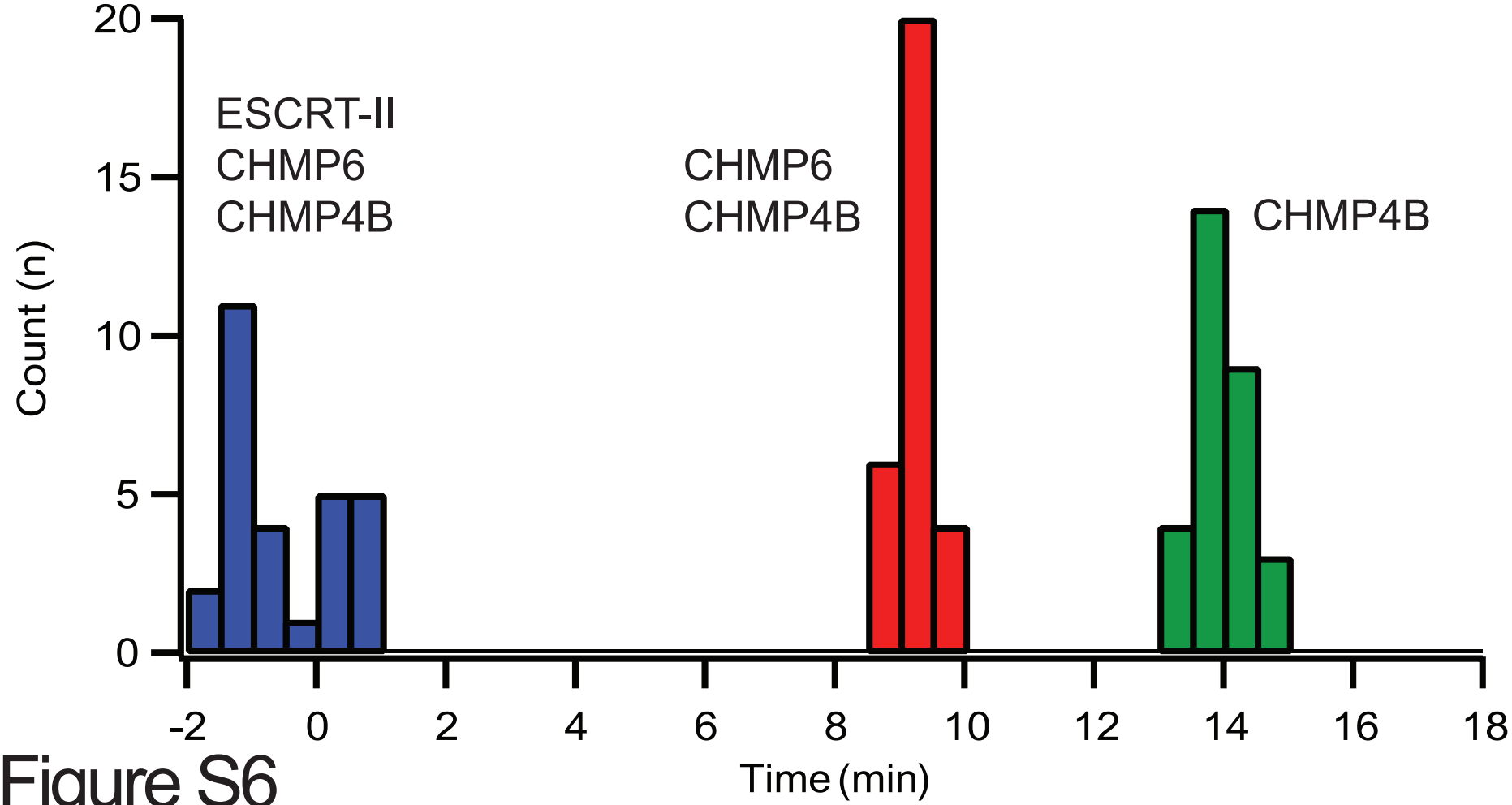
20
15
10
5
0
Count (n)
ESCRT-II
CHMP6
CHMP4B
CHMP6
CHMP4B
CHMP4B
-2
0
2
4
6
8
10
12
14
16
18
Time (min)

Figure S6

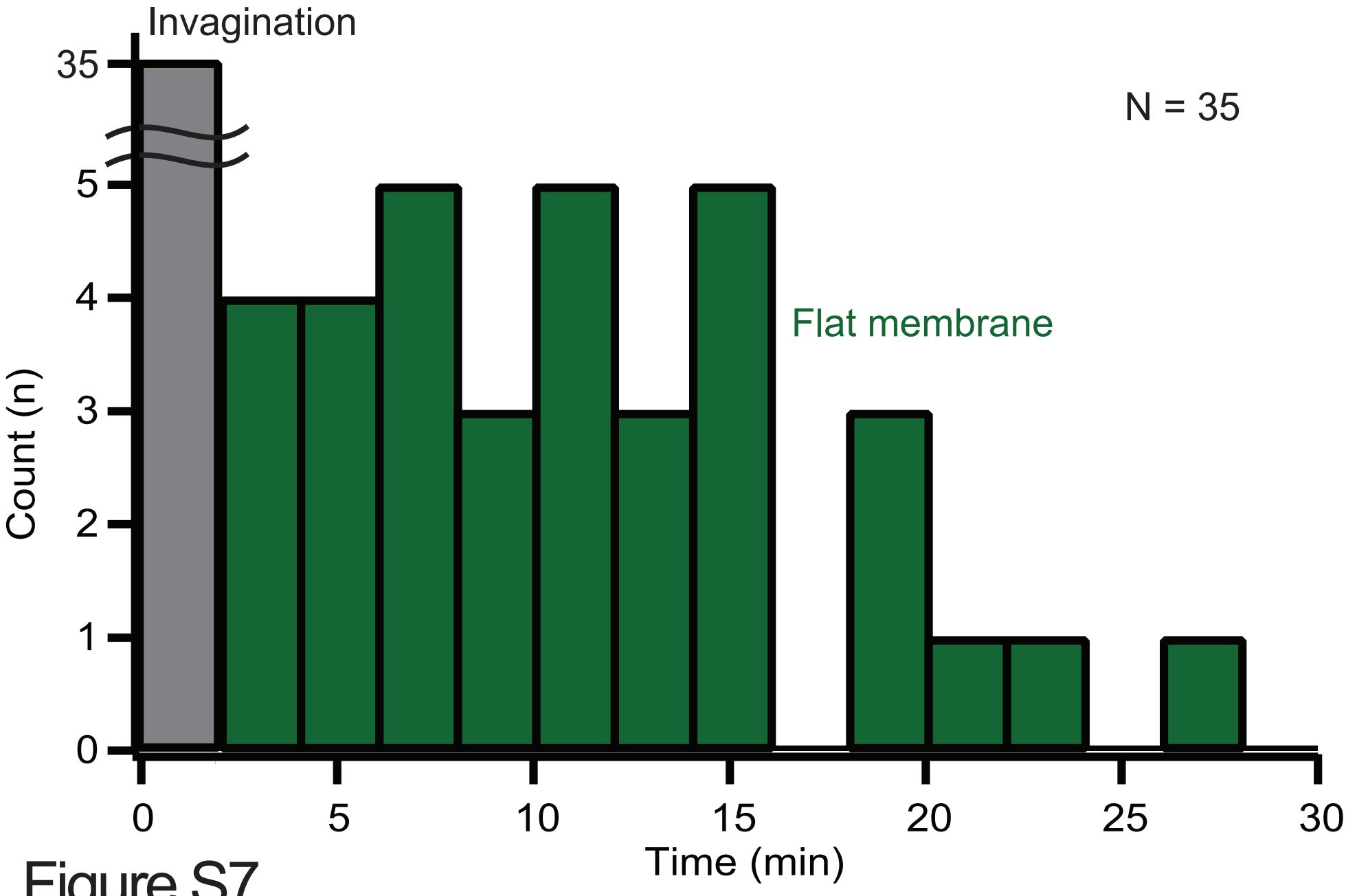
Invagination
35
5
4
3
2
1
0
N = 35
Flat membrane
Count (n)
0
5
10
15
20
25
30
Time (min)

Figure S7

Snf7 SIM

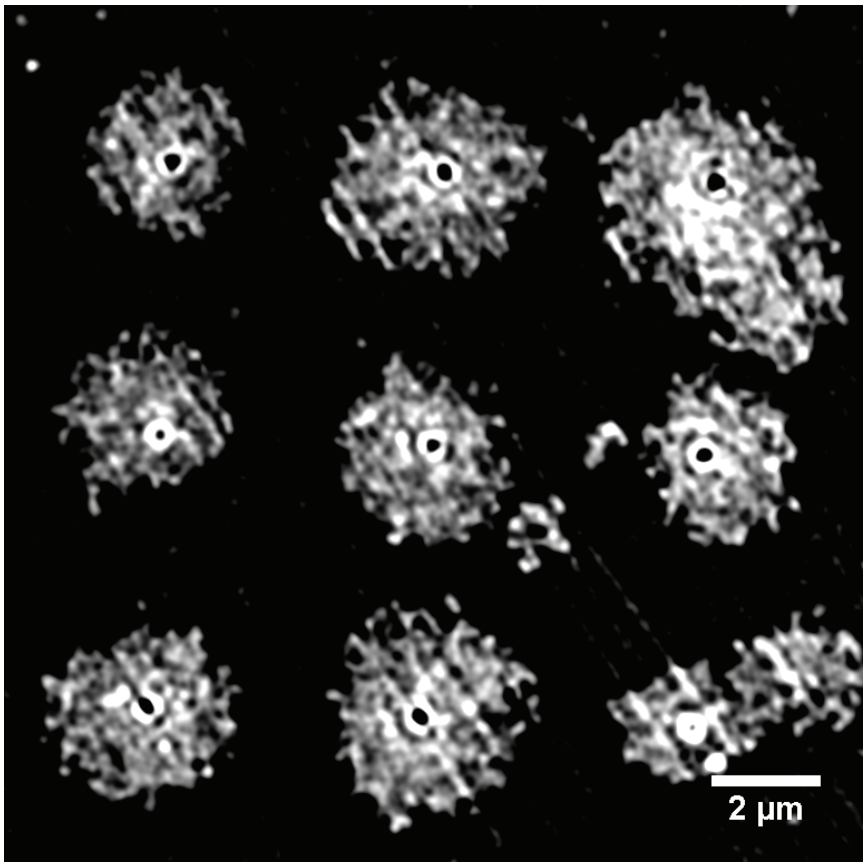

Image 1

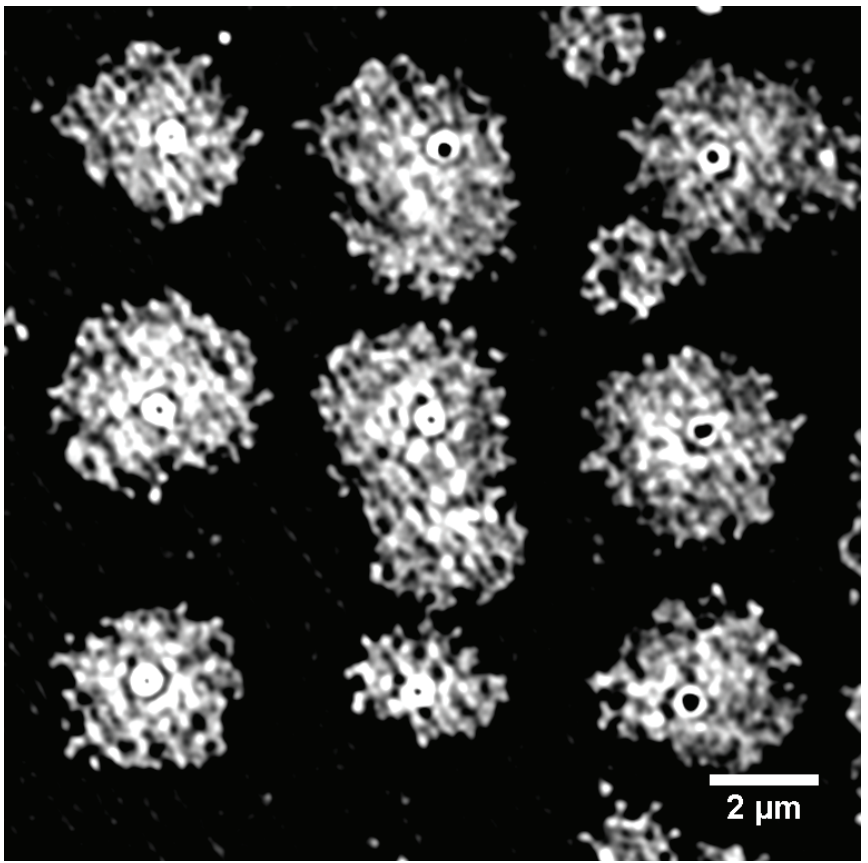

Image 2

Figure S8

Table S1. Parameters for concentration dependence of CHMP4 assembly

	ESCRT-II (nM)	CHMP6 (nM)	CHMP4B (nM)	K (10^{-3})	k_n (10^{-5} min^{-1})	k_e (10^{-1} min^{-1})	A_{tot} (Unitless)
Experiment 1	100	200	4	3.83	12.6	15.4	45
Experiment 2	100	200	40	51.3	4.01	1.79	300
Experiment 3	100	200	400	226	3.83	2.48	1300

The first three columns indicate the concentration of each protein used in the experiment, and the final four columns show kinetic parameters obtained by optimizing the mathematical model (Equation 1-2) to fit the data from each experiment.

Table S2. Parameters for CHMP6 and ESCRT-II dependence of CHMP4 assembly

	ESCRT-II (nM)	CHMP6 (nM)	CHMP4B (nM)	K (10^{-3})	k_n (10^{-5} min^{-1})	k_e (10^{-1} min^{-1})	A_{tot} (Unitless)
Experiment 1	0	0	40	0.0114	9.85	1.20	255
Experiment 2	0	200	40	2.18	5.56	0.962	310
Experiment 3	100	200	40	335	8.12	3.18	500

Concentrations and kinetic parameters are as described for Table 1.